

UC San Diego

UC San Diego Previously Published Works

Title

Efficient non-degenerate two-photon excitation for fluorescence microscopy.

Permalink

<https://escholarship.org/uc/item/73c9g1ww>

Journal

Optics Express, 27(20)

ISSN

1094-4087

Authors

Sadegh, Sanaz
Yang, Mu-Han
Ferri, Christopher GL
[et al.](#)

Publication Date

2019-09-30



DOI

10.1364/oe.27.028022

Peer reviewed



Efficient non-degenerate two-photon excitation for fluorescence microscopy

SANAZ SADEGH,^{1,10,*}  MU-HAN YANG,^{2,10} CHRISTOPHER G. L. FERRI,^{1,10} MARTIN THUNEMANN,¹ PAYAM A. SAISAN,¹ ZHE WEI,³ ERIK A. RODRIGUEZ,⁴  STEPHEN R. ADAMS,⁵ KIVILCIM KILIÇ,¹ DAVID A. BOAS,⁶ SAVA SAKADŽIĆ,⁷ ANNA DEVOR,^{1,7,8,11} AND YESHAIAHU FAINMAN^{9,11}

¹Department of Neurosciences, University of California, San Diego, CA 92093, USA

²Electrical and Computer Engineering Graduate Program, UCSD, La Jolla, CA 92093, USA

³Bioengineering Undergraduate Program, UCSD, La Jolla, CA 92093, USA

⁴Department of Chemistry, The George Washington University, Washington, DC 20052, USA

⁵Department of Pharmacology, University of California, San Diego, CA 92093, USA

⁶Department of Biomedical Engineering, Boston University, Boston, MA 02215, USA

⁷Martinos Center for Biomedical Imaging, MGH, Harvard Medical School, Charlestown, MA 02129, USA

⁸Department of Radiology, University of California, San Diego, CA 92093, USA

⁹Electrical and Computer Engineering Graduate Program, UCSD, La Jolla, CA 92093, USA

¹⁰These authors contributed equally to this study

¹¹These senior authors equally contributed to this study

*ssadegh@ucsd.edu

Abstract: Non-degenerate two-photon excitation (ND-TPE) has been explored in two-photon excitation microscopy. However, a systematic study of the efficiency of ND-TPE to guide the selection of fluorophore excitation wavelengths is missing. We measured the relative non-degenerate two-photon absorption cross-section (ND-TPACS) of several commonly used fluorophores (two fluorescent proteins and three small-molecule dyes) and generated 2-dimensional ND-TPACS spectra. We observed that the shape of a ND-TPACS spectrum follows that of the corresponding degenerate two-photon absorption cross-section (D-TPACS) spectrum, but is higher in magnitude. We found that the observed enhancements are higher than theoretical predictions.

© 2019 Optical Society of America under the terms of the [OSA Open Access Publishing Agreement](#)

1. Introduction

Two-photon microscopy [1] has had an enormous influence on biological studies providing a tool for high-resolution imaging hundreds of microns within live tissues. In neuroscience, two-photon imaging has been employed to trace neuronal connections [2], monitor biochemical signaling pathways [3], map protein distributions within individual cells and across cell populations [4], report gene expression [5,6], image oxygenation [7,8] and blood flow [9], trace neuronal circuits and image neuronal activity [10], and more. These studies relied on protein-based or synthetic fluorescent reporter molecules (hereafter referred to as fluorophores) suitable for two-photon excitation (TPE) [11].

In conventional two-photon microscopy, a fluorophore is excited by the simultaneous absorption of two photons of the same energy within the near-infrared (NIR) spectrum, derived from the same pulsed laser beam. This is called degenerate two-photon excitation, D-TPE. Alternatively, the same energy needed for the transition to the excited state can be delivered via absorption of two photons of different energy (i.e., different color) [12]. This non-degenerate two-photon excitation (ND-TPE) regime has been explored in two-photon excitation microscopy aiming to extend the excitation wavelength range [12–14], reduce out-of-focus fluorescence [15–18], increase spatial resolution [19,20], and increase penetration depth in scattering media [21,22].

The probability of two-photon excitation, quantified as the excitation cross-section, is an important parameter that, for a given fluorophore concentration and imaging conditions, translates into the laser power required for illumination [23]. However, a systematic study of non-degenerate two-photon absorption cross section (ND-TPACS) spectra of biologically relevant fluorophores, as a function of different combinations of excitation wavelengths, is missing. In addition, for deep imaging in biological tissue (e.g., live brain imaging), the choice of excitation wavelengths needs to be informed by considering the spectrum of water absorption and associated tissue heating.

Here, we performed ND-TPE spectroscopy of two fluorescent proteins (enhanced green fluorescent protein (EGFP) [24] and monomeric Kusabira orange 2 (mKO₂) [25]) and three organic dyes (Fluorescein [26], Coumarin 343 [27] and Sulforhodamine 101 (SR101) [28]) using a sensitive fluorescence excitation technique described in our recent study [29]. Further, we explored water absorption and tissue scattering as additional considerations for the selection of the excitation wavelengths for efficient ND-TPE, and compared tissue heating under different excitation regimes using heat conduction simulations.

2. Results

We quantified the ratio of the non-degenerate two-photon absorption cross section (ND-TPACS) to the best achievable degenerate two-photon absorption cross section (D-TPACS) within the equivalent range of the total photon energy (referred to thereafter as peak D-TPAC). In this way, we mitigated the need to measure the collection efficiency of our system at the expense of quantifying the absolute value of the ND-TPACS (see Appendices A, B, and C for experimental setup, spectroscopy protocol, and sample preparation). Plotting ND-TPACS normalized by peak D-TPACS as a function of near-infrared (NIR) and infrared (IR) wavelengths, λ_{NIR} and λ_{IR} respectively, generated a 2-dimensional ND-TPACS spectrum for each examined fluorophore within the available tuning range of the system (Fig. 1(a)). The highest ND-TPACS was obtained when the sum of NIR and IR photon energies matched the ground-to-excited state transition energy. In Fig. 1(a), the excitation energy isocline, a line connecting points with equal total energy ($E_{\text{NIR}} + E_{\text{IR}}$) on the 2-dimensional spectrum plot corresponding to the transition energy, is overlaid on the ND-TPACS spectrum for each fluorophore.

In Fig. 1(b), normalized D-TPACS of the five measured fluorophores along with ND-TPACS normalized to the peak D-TPACS are plotted as a function of the equivalent degenerate wavelength λ_{D} , where $2hc/\lambda_{\text{D}} = hc/\lambda_{\text{NIR}} + hc/\lambda_{\text{IR}}$ (h is the Planck constant, c is the speed of light in vacuum, and we have assumed equal refractive indices). In this way, we generated a linearized ND-TPACS spectrum that can readily be compared to the corresponding D-TPACS spectrum. Independently measured D-TPACS spectra were similar to the previously reported spectra of the fluorophores [23,30–32]. Several combinations of IR and NIR wavelengths correspond to the same equivalent degenerate wavelength (energy isoclines). Therefore, we report several ND-TPACS values (red dots) for each equivalent wavelength in Fig. 1(b). For each measured fluorophore, the shape of the linearized ND-TPACS spectrum was highly correlated with the D-TPACS spectrum for the longer wavelength region (Fig. 1(b)). However, we observed different amounts of enhancement, as indicated by different range of ND-TPACS values across different fluorophores. The measured fluorescent proteins have a larger spread in ND-TPACS values compared to the measured organic dyes. This might be because fluorescent proteins have a more complex molecular structure. Further studies are required to identify the mechanism behind this phenomenon.

In all examined cases, we observed an enhancement in ND-TPACS (red dots) compared to D-TPACS (black curves); a few red dots below the black curves fall well within our experimental measurement error (15% relative error, as shown in Appendix B). The observed enhancement in ND-TPACS, compared to D-TPACS, is partially due to the resonance enhancement effect [33–36]: when the energy difference between the high-energy incident photon ($\hbar\omega_{\text{NIR}}$ in our experiment, where $\omega_{\text{NIR}} = 2\pi c/\lambda_{\text{NIR}}$ is the frequency of the NIR beam) and that of the nearest

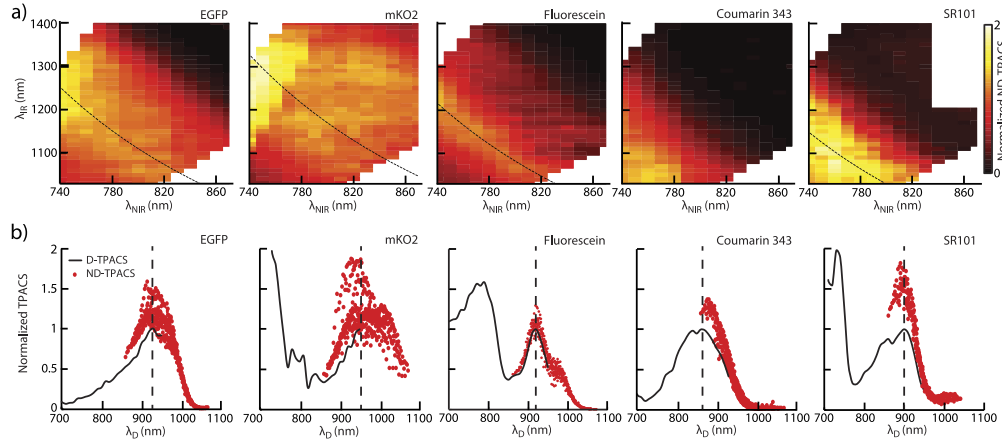


Fig. 1. ND-TPE spectroscopy. a) Color-coded, normalized ND-TPACS spectra for EGFP, mKO2, Fluorescein, Coumarin 343, and SR101 showing the dependence of the normalized ND-TPACS on NIR and IR wavelengths. The ND-TPACS at each combination of wavelengths was normalized by the peak D-TPACS value of the fluorophore. The isoclines corresponding to the ground to excited state transition energy ($hc/\lambda_{\text{NIR}} + hc/\lambda_{\text{IR}} = 2.66$ eV for EGFP, 2.6 eV for mKO2, 2.7 eV for Fluorescein, and 2.76 eV for SR101) are overlaid as dashed black lines. b) ND-TPACS normalized by the peak D-TPACS as a function of the equivalent degenerate wavelength $2/\lambda_{\text{D}} = 1/\lambda_{\text{NIR}} + 1/\lambda_{\text{IR}}$ are shown in red. Along any energy isocline, multiple excitation wavelength combinations within our tuning range sum to the same total energy and, therefore, the same equivalent wavelength. Thus, for each λ_{D} value we report several values of ND-TPACS (red dots). Independently measured D-TPACS normalized by its peak within the equivalent range of the total photon energy (2.3 – 2.9 eV) are shown in black. The black dashed vertical line indicates the position of the peak D-TPACS used for the normalization procedure (930 nm for EGFP, 950 nm for mKO2, 920 nm for Fluorescein, 860 nm for Coumarin 343, and 900 nm for SR101). These wavelengths correspond to the energy isoclines shown in panel (a).

one-photon allowed state is decreased, the probability of ND-TPE increases due to a longer lifetime of the reached virtual state as compared to the virtual state corresponding to D-TPE. In other words, the probability of two-photon absorption is proportional to the lifetime of the virtual intermediate excited state, which is inversely proportional to the energy difference between the closest one-photon allowed state and the virtual state [33–36]. This energy difference is called detuning energy Δ , which is maximal in the case of D-TPACS, where the virtual state is in the middle between ground and first excited state. Therefore, for excitation to a specific excited state, D-TPA has a lower probability of occurrence compared to ND-TPA. The detuning energy, in case of excitation into the lowest excited state, is equal to the energy of the low-energy incident photon $\hbar\omega_{\text{IR}}$, where ω_{IR} is the frequency of the IR beam. Since all five measured fluorophores are non-centrosymmetric, two-photon absorption is allowed to the lowest excited state. Therefore, we are particularly interested in the case where one of the incident photons approaches the resonance with the lowest one-photon allowed state, known as intermediate state resonance enhancement (ISRE). Using the 2-level essential-state approximation of the sum-over-states (SOS) model, we find that the relation between $\Delta = \hbar\omega_{\text{IR}}$ and ISRE_2 for non-centrosymmetric fluorophores is given by the following formula (see Appendix D):

$$\text{ISRE}_2 = \frac{\sigma_{\text{ND}}(\omega_{\text{NIR}}, \omega_{\text{IR}})}{\sigma_{\text{D}}(\omega_{\text{D}})} = \frac{(\hbar\omega_{\text{NIR}} + \hbar\omega_{\text{IR}})^2}{4\hbar\omega_{\text{NIR}}\hbar\omega_{\text{IR}}} \quad (1)$$

where we have assumed that $2\hbar\omega_D = \hbar\omega_{\text{NIR}} + \hbar\omega_{\text{IR}}$ or, in other words, ISRE_2 is the fractional change of ND-TPACS relative to D-TPACS at the equivalent degenerate frequency. From Eq. (1), one finds that ISRE_2 increases asymptotically as the energy of the IR photon approaches zero, $\hbar\omega_{\text{IR}} \rightarrow 0$, or, equivalently, when the energy of the NIR beam approaches the transition energy, $\hbar\omega_{\text{NIR}} \rightarrow 2\hbar\omega_D$. In Table 1, we show experimental and theoretical ISRE_2 values calculated using Eq. (1) for four fluorophores, where the measurements were performed along the isoclines corresponding to the respective lowest excited state (see Fig. 7 for the graphical representation of Table 1). Assuming a constant total transition energy, ISRE_2 increases by decreasing the detuning energy, as expected. We observe that, within our estimated 15% relative experimental error, most of the experimental values of the ISRE are higher than those predicted by 2-level approximation of the SOS model given by Eq. (1). Adding more intermediate states to the essential-state approximation might increase the predicted enhancement. In Appendix D, we derive the formalism for the 3-level approximation of the SOS model (ISRE_3 given by Eq. 11). An explicit calculation ISRE_3 would require knowledge of the transition and permanent dipole moments of the fluorophores that currently are unknown. Using the 2-level model, as the simplest approximation, is the limitation of our approach for calculating a theoretical prediction of the enhancement. Additional enhancement of ND-TPACS may also be due to the participation of low-lying vibronic transitions, having very low transition dipole moments associated with them and thus not readily observable in the linear absorption spectra. Within our available tuning range, we achieve enhancement in the ND-TPACS of up to $\sim 75\%$ for mKO2 (Fig. 1). Higher enhancement values would be achieved by further decreasing the detuning energy, as long as that energy is larger than the natural bandwidth of the first one-photon excited state transition [34]. At the limit where the energy of the incident high-energy photon is within the natural bandwidth of the transition, fluorescence from single photon excitation dominates over multiphoton excited fluorescence, negating all advantages of multiphoton excitation.

Table 1. Comparison between experimental and theoretical (two-level approximation, Eq. (1)) values of the ISRE_2 for $\hbar\omega_{\text{NIR}} + \hbar\omega_{\text{IR}} = 2.66$ eV for EGFP, 2.6 eV for mKO2, 2.7 eV for Fluorescein, and 2.76 eV for SR101. (See Fig. 7 for the graphical representation of the results)

EGFP				mKO2			
$\hbar\omega_{\text{NIR}}$	$\hbar\omega_{\text{IR}}$	ISRE_2	$\text{ISRE}_{\text{experiment}}$	$\hbar\omega_{\text{NIR}}$	$\hbar\omega_{\text{IR}}$	ISRE_2	$\text{ISRE}_{\text{experiment}}$
1.33	1.33	1.000	–	1.30	1.30	1.000	–
1.51	1.15	1.019	1.1 ± 0.2	1.49	1.11	1.022	1.0 ± 0.2
1.63	1.03	1.054	1.4 ± 0.2	1.55	1.05	1.038	1.2 ± 0.2
1.67	0.99	1.070	1.5 ± 0.2	1.63	0.97	1.069	1.6 ± 0.2
Fluorescein				SR101			
$\hbar\omega_{\text{NIR}}$	$\hbar\omega_{\text{IR}}$	ISRE_2	$\text{ISRE}_{\text{experiment}}$	$\hbar\omega_{\text{NIR}}$	$\hbar\omega_{\text{IR}}$	ISRE_2	$\text{ISRE}_{\text{experiment}}$
1.35	1.35	1.000	–	1.38	1.38	1.000	–
1.53	1.17	1.018	1 ± 0.2	1.55	1.21	1.015	1.2 ± 0.2
1.61	1.09	1.039	1.1 ± 0.2	1.61	1.15	1.029	1.4 ± 0.2
1.68	1.02	1.064	1.3 ± 0.2	1.66	1.10	1.043	1.4 ± 0.2

The knowledge of ND-TPACS alone may be enough to guide the choice of wavelengths for imaging relatively thin and transparent samples. For deep imaging in live biological tissues, however, this choice is affected by other considerations, such as light scattering, water absorption, and the associated heating of the sample. In Fig. 2(a), we show the effects of water absorption, and tissue scattering for different wavelengths (adapted from [21] with permission). Longer wavelengths undergo lower scattering in tissue; however, as shown in Fig. 2(a), water absorption increases significantly at wavelengths near 1500 nm and beyond 1800 nm. Higher water

absorption at longer wavelengths will result in greater tissue heating. In ND-TPE, the IR beam has longer wavelengths compared to D-TPE, and excessive tissue heating is a potential concern for ND-TPE, even when equal total excitation power is used. However, it has been shown that the increase in tissue temperature is much smaller than the increase of the water absorption coefficient [37] and therefore, the increase in tissue heating for longer wavelengths is not as drastic as expected. This is also evident in tissue heating simulations shown in Fig. 2(b), where we plot the maximum temperature change of the sample when illuminated by both NIR and IR beams, $\Delta T_{\text{NIR+IR}} = \Delta T_{\text{NIR}} + \Delta T_{\text{IR}}$, relative to the maximum temperature change upon illumination with a single beam at the equivalent degenerate wavelength, ΔT_{D} , assuming equal total powers (see Appendix E for the description of the simulation). For example, the ratio of the water absorption coefficient at 1340 nm to the absorption coefficient at 920 nm is ~ 30 (red plot in Fig. 2(a) and Table 3), but the ratio of the temperature change between D-TPE with $\lambda_{\text{D}} = 920$ nm and ND-TPE with $\lambda_{\text{NIR}} = 700$ nm and $\lambda_{\text{IR}} = 1340$ nm and equal excitation power is ~ 3 . This result agrees with the idea that most of the incident light is absorbed before escaping the thick tissue sample and therefore, the variation in the absorption coefficient of different wavelengths does not drastically affect the rate of tissue heating [37].

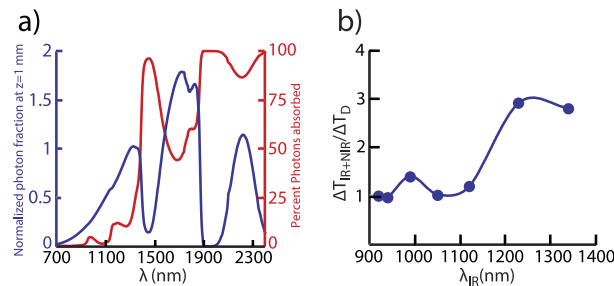


Fig. 2. Choice of excitation wavelengths in ND-TPE microscopy. a) Effects of scattering and absorption (adapted from [21]): photon fraction at depth of 1 mm, considering both absorption and scattering, for average brain tissue optical properties is shown as blue line. Percent of the photons absorbed by brain tissue in 1 mm is shown as red line. b) Simulation results for tissue heating by a scanned focused light: ratio of the maximum tissue temperature change under simultaneous excitation by NIR and IR beam to maximum temperature change under excitation with a single beam with equivalent degenerate wavelength, $2hc/\lambda_{\text{D}} = hc/\lambda_{\text{NIR}} + hc/\lambda_{\text{IR}}$ and $\lambda_{\text{D}} = 920$ nm, versus λ_{IR} assuming equal total excitation power $P_{\text{NIR}} + P_{\text{IR}} = P_{\text{D}} = 100$ mW at focal point ($250 \mu\text{m}$ below surface).

3. Conclusion

In conclusion, we showed that, within our measured excitation range, the ND-TPACS spectrum of all fluorophores tested follow their corresponding D-TPACS in shape and exhibit enhancement in magnitude. We showed that the amount of the observed enhancement is higher than the theoretical prediction given by the 2-level essential-state approximation of the SOS model. Different fluorophores exhibit different amounts of resonance enhancement and we observed up to $\sim 75\%$ enhancement in the ND-TPACS compared to the corresponding D-TPACS. We also showed that the increase in tissue heating, due to excitation with longer wavelengths, is not as large as water absorption increase for longer wavelengths. This increase in heating may be an acceptable trade-off for leveraging enhanced ND-TPACS and other advantages of ND-2PE [22] in deep tissue imaging applications.

Appendix A: Experimental setup

Detailed description of the spectroscopy setup is found in our recent work [29]. In brief, two temporally synchronized and spatially aligned pulsed femtosecond laser beams, one with near infrared (NIR) and another with infrared (IR) energies, were derived from a Ti:Sapphire laser and optical parametric oscillator (OPO), respectively. The beams, linearly polarized in the same plane, were combined on a dichroic mirror and focused by a microscope objective (Olympus, LMPLN-10X-IR, NA=0.3) into the sample solution (Fig. 3(a)). The NIR and IR wavelengths were scanned in 10 nm increments in the range of 740 – 870 nm and 1100 – 1400 nm, respectively. We measured and recorded the fluorescence intensity and the following parameters for each laser beam: wavelength, spectral pulse bandwidth, average power, and repetition rate. The NIR optical path included a delay stage, so that the time-averaged intensity of the fluorescence could be measured as a function of the temporal delay between the NIR and IR pulses (Fig. 3(b)). All measurements were conducted at sufficiently low incident powers, ensuring that two-photon excitation was the only mechanism that generated the fluorescence signal and other non-linear phenomena such as stimulated emission and excited-state absorption are absent [29]. To show that the ND-TPE was the only fluorescence excitation mechanism, we plotted the fluorescence signal value at the peak of the temporal overlap (fluorescence generated by both ND-TPE and D-TPE) minus the fluorescence signal at no temporal overlap (fluorescence generated by D-TPE) as a function of the excitation power of each individual beam as shown in Fig. 4. The linear dependence of the fluorescence signal generated by ND-TPE on the excitation power of each beam is the characteristic signature of the ND-TPE [22,29].

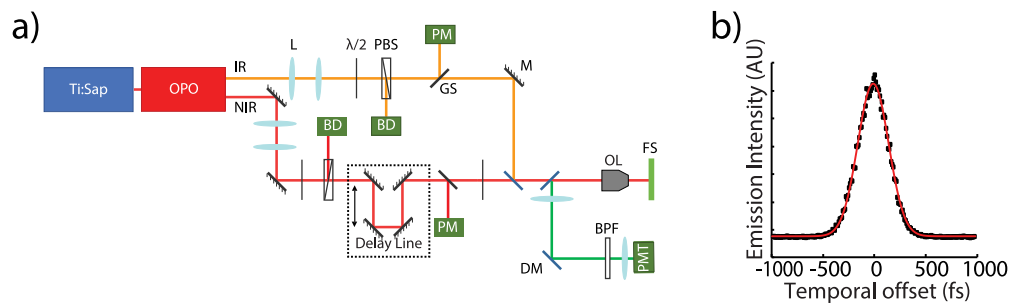


Fig. 3. a) Experimental setup for ND-TPACS measurement. L, lens; PBS, polarizing beam splitter; $\lambda/2$, half wave plate; GS, glass slide; M, mirror; DM, dichroic mirror; BD, beam dump; FS, fluorescent sample; OL, objective lens; BPF, band pass filter; PM, power meter; and PMT, photomultiplier tube. b) A typical plot of fluorescence intensity as a function of the temporal offset between NIR and IR pulses. The increase in the signal at zero temporal offset is due to ND-TPE. The red line shows the fitted model (Eq. (3)).

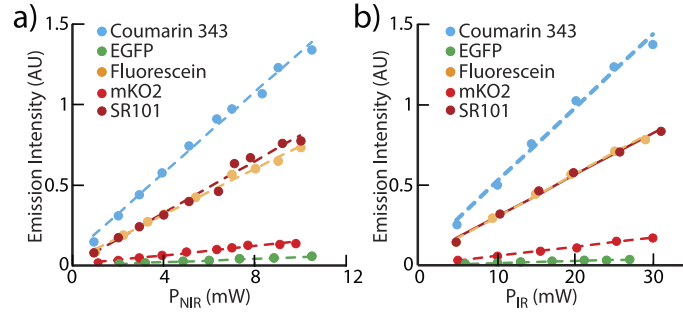


Fig. 4. Linear dependence of non-degenerate two-photon fluorescence excitation on a) NIR excitation power ($P_{\text{IR}} = 15$ mW), and b) IR excitation power ($P_{\text{NIR}} = 5$ mW). The power dependence was tested at wavelength combinations $\lambda_{\text{NIR}} = 740$ nm and $\lambda_{\text{IR}} = 1230$ nm for all measured fluorophores.

Appendix B: Spectroscopy protocol

The fluorescence intensity measured as a function of the delay-line position (Fig. 3(b)), resulted in a cross-correlation curve that was generated for each combination of NIR and IR wavelengths (Fig. 3(b)). When NIR and IR pulses arrived at different times (Temporal offset >0), the fluorescence signal was generated by degenerate two-photon excitation (D-TPE) due to absorption of two photons of equal energy coming from either the NIR or IR beam. An increase in the fluorescence signal was detected as laser pulses from the two beams overlapped in time indicating the additive effect of the non-degenerate two-photon excitation (ND-TPE) occurring due to simultaneous absorption of one photon from each NIR and IR beam. To isolate the ND-TPE signal, for each combination of NIR and IR wavelengths, we subtracted the D-TPE contribution from the fluorescence intensity at zero delay between NIR and IR pulses. Next, we compared the probability of two-photon absorption between D-TPE and ND-TPE. In D-TPE, the time-averaged fluorescence signal can be expressed as the following equation:

$$\langle F \rangle_{\text{D}} = \frac{\sqrt{\pi} C P^2 \lambda \phi \eta \sigma_{\text{D}}^{(2)}(\lambda)}{4 f c^2 h^2 \Gamma}. \quad (2)$$

where C is the concentration of the fluorophore, P is the laser power, λ is the laser beam wavelength, η is the quantum efficiency of the fluorophore, ϕ is the collection efficiency of the measurement system, $\sigma_{\text{D}}^{(2)}(\lambda)$ is the degenerate two-photon absorption cross-section (D-TPACS) at wavelength λ , f is the laser repetition rate, c is the speed of light, h is the Planck's constant, and Γ is the temporal width of the laser pulse [29]. When excited with NIR and IR laser beams, the time-averaged fluorescence signal is a sum of fluorescence generated by ND-TPE and fluorescence generated by D-TPE due to absorption of either the NIR or IR beam alone and is given by the following equation:

$$\begin{aligned} \langle F(\tau) \rangle = & \frac{\sqrt{\pi} C P_{\text{NIR}}^2 \lambda_{\text{NIR}} \phi \eta \sigma_{\text{D}}^{(2)}(\lambda_{\text{NIR}})}{4 f c^2 h^2 \Gamma_{\text{NIR}}} + \frac{\sqrt{\pi} C P_{\text{IR}}^2 \lambda_{\text{IR}} \phi \eta \sigma_{\text{D}}^{(2)}(\lambda_{\text{IR}})}{4 f c^2 h^2 \Gamma_{\text{IR}}} \\ & + \frac{2 \sqrt{\pi} C P_{\text{NIR}} P_{\text{IR}} \lambda_{\text{NIR}} \lambda_{\text{IR}} \phi \eta \sigma_{\text{ND}}^{(2)}(\lambda_{\text{NIR}}, \lambda_{\text{IR}})}{f c^2 h^2 \Gamma_x \sqrt{\lambda_{\text{NIR}}^2 + \lambda_{\text{IR}}^2}} \exp\left(\frac{-\tau^2}{2 \Gamma_x^2}\right). \end{aligned} \quad (3)$$

where τ is the temporal offset, P_{NIR} and P_{IR} are the laser power of the NIR and IR beams, λ_{NIR} and λ_{IR} are the wavelengths of the NIR and IR beams, $\sigma_{\text{ND}}^{(2)}(\lambda_{\text{NIR}}, \lambda_{\text{IR}})$ is the non-degenerate

two-photon absorption cross-section (ND-TPACS) at a specific combination of NIR and IR wavelengths λ_{NIR} and λ_{IR} , Γ_{NIR} and Γ_{IR} are the temporal width of the NIR and IR beams, and Γ_x is the temporal width of the cross-correlation curve of the NIR and IR laser pulses [29]. The first two terms of Eq. (3) are the fluorescence from D-TPE for each one of the beams. These terms are constant with respect to pulse delay and appear as a constant fluorescence background. By acquiring the fluorescence intensity as a function of relative pulse delay, we can measure both the ND-TPACS and D-TPACS by fitting this model to the data, assuming that all other parameters including fluorophore concentration, fluorescence quantum efficiency, and collection efficiency are known [29].

Measurement of the absolute ND-TPACS would require knowledge of the fluorophore quantum efficiency η and the collection efficiency of the measurement system ϕ . Our goal, however, was to compare ND-TPE to D-TPE and evaluate the possibility of enhancement of two-photon absorption upon ND-TPE. Therefore, for each fluorophore, we quantified the ratio of ND-TPACS to the peak (i.e., the best achievable) D-TPACS and not the absolute value of ND-TPACS. To that end, we normalized all ND-TPACS measurements by the peak D-TPACS, which occurred at the wavelength where the photon energy matched half of the total energy needed for the transition to the excited state. This is because under D-TPE, two photons are drawn from the same beam and have the same photon energy. D-TPACS was independently measured within the same range of the total energy of two photons by blocking the IR beam. This normalization mitigated the need to explicitly measure ϕ and η , because these terms disappear when dividing Eq. (3) by Eq. (2). For each fluorophore, the normalized ND-TPACS spectrum was computed by fitting cross-correlation curves (Fig. 3(b)) with Eq. (3) for each pair of NIR and IR wavelengths and normalizing the obtained value by the peak D-TPACS that is a fluorophore-specific constant. For a more detailed description of the spectroscopy protocol please refer to our recent work on the spectroscopy technique [29]. We characterized the measurement error via repetitive measurement of the ND-TPACS along one isocline (Fig. 5). The main source of error was the uncertainty in the measurement of IR beam pulse width, fluorescence signal value, and laser powers.

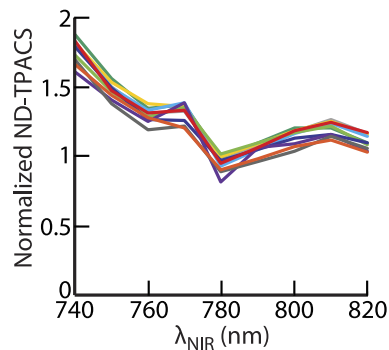


Fig. 5. Characterization of the experimental error in ND-TPACS measurements via repetitive measurements of ND-TPACS along one isocline. Here we show 10 measurements of normalized ND-TPACS of EGFP along the $hc/\lambda_{\text{NIR}} + hc/\lambda_{\text{IR}} = 2.66$ eV isocline vs λ_{NIR} . The measured relative experimental error is $\sim 15\%$.

Appendix C: Sample preparation

Fluorophores were dissolved in phosphate-buffered saline (PBS, pH ~ 7.4) or dimethyl sulfoxide (DMSO) to final concentrations listed in Table 2. The concentrations were measured using one-photon absorption spectroscopy (NanoDrop 2000 spectrometer, ThermoFisher) and published

molar extinction coefficients. One photon-absorption spectra of inspected fluorophores are shown in Fig. 6.

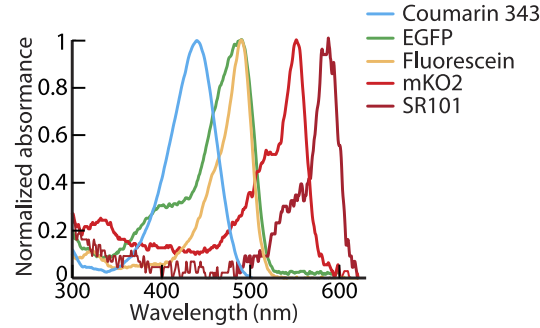


Fig. 6. Normalized one-photon absorption spectra of Coumarin 343 (cyan), EGFP (green), Fluorescein (yellow), mKO2 (red), and SR101 (dark red).

Table 2. Fluorophore concentrations.

Fluorophores	Solvent	Extinction Coefficient $M^{-1}mm^{-1}$	Concentration μM
Fluorescein	PBS	7500 [38]	90
EGFP	PBS	5600 [38]	45
mKO2	PBS	6380 [39]	20
SR101	PBS	13900 [40]	5
Coumarin 343	DMSO	4430 [27]	135

Appendix D: Derivation of the intermediate state resonance enhancement (ISRE)

In this section we derive the formula for ISRE₂ (Eq. (1) in the main text). We start with the expression for TPA tensor $\mathbf{S}^{(f)}$ for the transition from ground state $|g\rangle$ to final state $|f\rangle$ which is given by:

$$|\mathbf{S}^{(f)}|^2 = \left| \sum_i \left[\frac{(\mathbf{e}_1 \cdot \boldsymbol{\mu}_{i0})(\boldsymbol{\mu}_{fi} \cdot \mathbf{e}_2)}{E_i - \hbar\omega_1 + i\xi_i} + \frac{(\mathbf{e}_1 \cdot \boldsymbol{\mu}_{i0})(\boldsymbol{\mu}_{fi} \cdot \mathbf{e}_2)}{E_i - \hbar\omega_2 + i\xi_i} \right] \right|^2, \quad (4)$$

where $\mu_{mn} = \langle m|\boldsymbol{\mu}|n\rangle$, i.e. vectors with components $(\mu_{mn}^x, \mu_{mn}^y, \mu_{mn}^z)$, are the element of the electric dipole operator $\boldsymbol{\mu}$; and \mathbf{e}_1 and \mathbf{e}_2 are the unit polarization vectors of the two photons with energies $\hbar\omega_1$ and $\hbar\omega_2$, respectively [41–43]. Index ‘ i ’ in Eq. (4) runs over intermediate states $|i\rangle$ with energies E_i including the ground state ($i = 0$) and the final state ($i = f$). The damping constant ξ_i is associated with the line shape (density of states) of the intermediate state and is commonly set (in calculations) to an arbitrary chosen small value. The relation between $\mathbf{S}^{(f)}$ and ND-TPACS is given by:

$$\sigma_{ND}(\omega_1, \omega_2) \sim \omega_1\omega_2 |\mathbf{S}^{(f)}|^2 \rho_f(\omega_{NIR} + \omega_{IR} - \omega_f), \quad (5)$$

where $\rho_f(\omega_{NIR} + \omega_{IR} - \omega_f)$ is the line shape function [41–43].

Let’s assume, for simplicity that all transitions are polarized in the same direction and this direction is parallel to the two polarization vectors \mathbf{e}_1 and \mathbf{e}_2 . This assumption will not affect the generality of the conclusions. Under this assumption, the $|\mathbf{S}^{(f)}|^2$ expression can be written in a

simpler form:

$$|\mathbf{S}^{(f)}|^2 = \left| \sum_i \left[\frac{\mu_{i0}\mu_{fi}}{E_i - \hbar\omega_1 + i\xi_i} + \frac{\mu_{i0}\mu_{fi}}{E_i - \hbar\omega_2 + i\xi_i} \right] \right|^2. \quad (6)$$

The full sum-over states (SOS) model considers the contribution of all excited (intermediate) states in the TPA tensor. However, in the essential-state approximation the full SOS treatment is truncated by assuming one strongly one-photon allowed state $|i\rangle$ that acts as intermediate state for TPA into two-photon allowed state $|f\rangle$. The essential-state model has been successfully applied for degenerate TPA calculations in a variety of fluorophores [44–46]. Research showed that the essential state model can effectively reproduce the converged full SOS model results for ISRE of two fluorene derivatives [34]. For non-centrosymmetric molecules, there is no formal mutual exclusion between the selection rules for one-photon and two-photon transitions $|i\rangle = |f\rangle$, and we have a 2-level system. Under the 2-level approximation of the SOS model the TPA tensor for non-centrosymmetric molecules can be written as:

$$|\mathbf{S}^{(f)}|^2 = \left| \left[\frac{\mu_{00}\mu_{f0}}{E_0 - \hbar\omega_1 + i\xi_0} + \frac{\mu_{00}\mu_{f0}}{E_0 - \hbar\omega_2 + i\xi_0} \right] + \left[\frac{\mu_{f0}\mu_{ff}}{E_f - \hbar\omega_1 + i\xi_f} + \frac{\mu_{f0}\mu_{ff}}{E_f - \hbar\omega_2 + i\xi_f} \right] \right|^2. \quad (7)$$

Here $E_0 = 0$, since this is our reference ground state energy. We can consider that the line broadening parameters ξ_0 , ξ_f and ξ_i are small compared to all the other energy terms. Therefore, for a resonance to the final state ($E_f = \hbar\omega_1 + \hbar\omega_2$) we have:

$$|\mathbf{S}^{(f)}|^2 \sim [\mu_{f0}(\mu_{ff} - \mu_{00})]^2 \left(\frac{1}{\hbar\omega_1} + \frac{1}{\hbar\omega_2} \right)^2. \quad (8)$$

It is easy to show analytically (or numerically) that Eq. (8) has its minimum when $\hbar\omega_1 = \hbar\omega_2$ (assuming constant transition energy $\hbar\omega_1 + \hbar\omega_2$). By inserting Eq. (8) into Eq. (5) we find the following simple scaling relation for ND-TPACS

$$\sigma_{\text{ND}}(\omega_1, \omega_2) \sim \frac{(\hbar\omega_1 + \hbar\omega_2)^2}{\hbar\omega_1 \hbar\omega_2}, \quad (9)$$

Therefore, the ISRE₂ is given by:

$$\text{ISRE}_2 = \frac{\sigma_{\text{ND}}(\omega_{\text{NIR}}, \omega_{\text{IR}})}{\sigma_{\text{D}}(\omega_{\text{D}})} = \frac{(\hbar\omega_{\text{D}})^2}{\hbar\omega_{\text{NIR}} \hbar\omega_{\text{IR}}} = \frac{(\hbar\omega_{\text{NIR}} + \hbar\omega_{\text{IR}})^2}{4\hbar\omega_{\text{NIR}} \hbar\omega_{\text{IR}}}, \quad (10)$$

where we have assumed $2\hbar\omega_{\text{D}} = \hbar\omega_{\text{NIR}} + \hbar\omega_{\text{IR}}$, or in other words, ISRE is the fractional change of ND-TPACS relative to D-TPACS at the equivalent degenerate frequency.

Using the same procedure as for the 2-level system given above, here we derived the ISRE for a 3-level system with $|i\rangle$ as the additional intermediate state:

$$\text{ISRE}_3 = \frac{\hbar\omega_{\text{NIR}} \hbar\omega_{\text{IR}} \left| \mu_{f0}(\mu_{00} - \mu_{ff}) \left(\frac{1}{\hbar\omega_{\text{NIR}}} + \frac{1}{\hbar\omega_{\text{IR}}} \right) + \mu_{i0}\mu_{fi} \left(\frac{1}{E_i - \hbar\omega_{\text{NIR}}} + \frac{1}{E_i - \hbar\omega_{\text{IR}}} \right) \right|^2}{(\hbar\omega_{\text{D}})^2 \left| \mu_{f0}(\mu_{00} - \mu_{ff}) \left(\frac{2}{\hbar\omega_{\text{D}}} \right) + \mu_{i0}\mu_{fi} \left(\frac{2}{E_i - \hbar\omega_{\text{D}}} \right) \right|^2}. \quad (11)$$

From Eq. (11) we can see that ISRE₃ calculation would require knowledge of permanent and transition dipole moments of the intermediate and final states of the fluorophores.

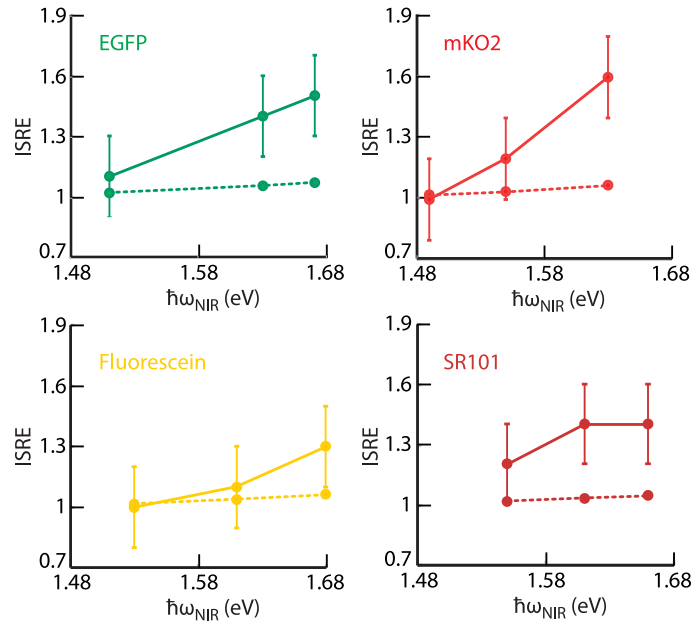


Fig. 7. Graphical representation of Table 1 for comparison of the experimental and theoretical (two-level approximation, Eq. (1)) values of the ISRE for $\hbar\omega_{\text{NIR}} + \hbar\omega_{\text{IR}} = 2.66$ eV for EGFP, 2.6 eV for mKO2, 2.7 eV for Fluorescein, and 2.76 eV for SR101. Experimental data (solid line) and theoretical results (dashed line) are overlaid.

Appendix E: Heating comparison

To study potential heating under ND-TPE, we simulate tissue heating through scanned focused light using a MATLAB code, which was provided by K. Podgorski [37]. The code uses Monte Carlo simulations to simulate light spread in tissue and the finite differencing method for heat conduction, metabolic heating, and cooling by blood perfusion [37]. The code assumes a heterogeneous sample incorporating a 350- μm glass window and immersion water above the sample [37]. The simulated focused beam is set to scan a 1 mm² area at 250 μm below the surface. We used previously published values for optical parameters of brain tissue [21,47] (Table S2). For simulation of heating under simultaneous excitation with NIR and IR beams, we used the code to simulate the heating under individual NIR and IR beams and then added the resulting tissue temperature changes to obtain the heating for the case that both beams are illuminating the sample at the same time. This is a viable approach since the superposition principle is valid for heat propagation which is described by a linear partial differential equation. Podgorski et al. showed that heating varies in different parts of the sample relative to the focal point and the temperature change is greatest deep below the brain surface and focal plane [37].

In Fig. 8(a) we show the spatial temperature profile of brain tissue in resting equilibrium and when illuminated using a NIR wavelength of 740 nm, an IR wavelength of 1230 nm and the equivalent degenerate wavelength of 920 nm ($2/\lambda_{\text{D}} = 1/\lambda_{\text{NIR}} + 1/\lambda_{\text{IR}}$). Light is focused and scanned 250 μm below the cover glass over a 1 mm² scan area. Power of the excitation beams were chosen such that $P_{\text{NIR}} + P_{\text{IR}} = P_{\text{D}} = 100$ mW and $P_{\text{NIR}} = P_{\text{IR}}$ at focal depth (250 μm below cover glass). For example, at $\lambda_{\text{NIR}} = 740$ nm we set $P_{\text{NIR}}(z = 250 \mu\text{m}) = 50$ mW at focal depth which means the input laser power at surface is $P_{\text{NIR}}(z = 0 \mu\text{m}) = 100 \times (P_{\text{NIR}}(z = 250 \mu\text{m})/T(\lambda_{\text{NIR}} = 740 \text{ nm}; z = 250 \mu\text{m})) = 250$ mW. Tissue exhibits the highest temperature change

when illuminated with the IR beam (Fig. 8(b)) as expected given high absorption of water at this wavelength.

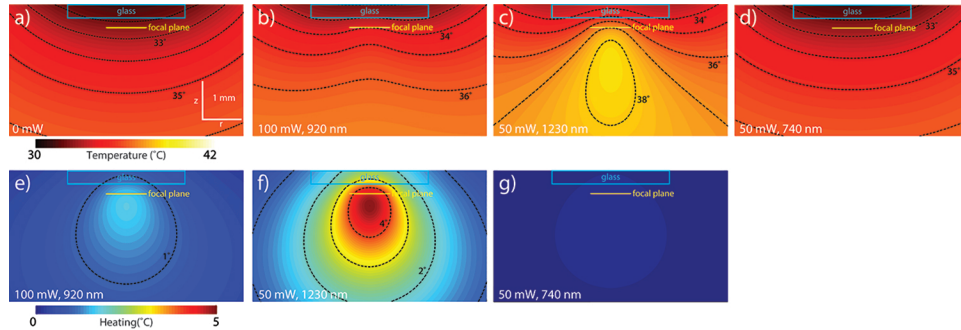


Fig. 8. Tissue heating simulations. Simulation code was provided by K. Podgorski [37]. a-d) Simulated spatial temperature profile in brain tissue with cover glass and immersion water (temperature of the immersion water 1 mm above cover glass was kept constant at 25 °C). Profiles are shown for no illumination, 100 mW at 920 nm, 50 mW at 1230 nm, and 50 mW at 740 nm. e-g) Simulated temperature change for 100 mW at 920 nm, 50 mW at 1230 nm, and 50 mW at 740 nm. Contour lines are shown for 1 °C intervals. All powers are given for a focal plane 250 μm below the surface.

Table 3. Optical parameters for average brain tissue [21,47] that were used in our heating simulations. μ_a and μ_s are the absorption and scattering coefficients, respectively, and $T = 100 \times e^{-(\mu_a + \mu_s)z}$ is the light transmission percentage at depth z . We set $z = 250 \mu\text{m}$ for our tissue heating simulations.

λ_{NIR} (nm)	μ_s (1/mm)	μ_a (1/mm)	T (%)	λ_{NIR} (nm)	μ_s (1/mm)	μ_a (1/mm)	T (%)
700	6.9	5×10^{-4}	18	1340	2.8	0.2	47
740	6.4	2.1×10^{-3}	20	1230	3.2	8.9×10^{-2}	44
780	6.0	2×10^{-3}	22	1120	3.6	1.9×10^{-2}	40
820	5.6	1.7×10^{-3}	25	1050	4.0	1.2×10^{-2}	37
860	5.2	3.3×10^{-3}	27	990	4.3	3.4×10^{-2}	34
900	4.9	4.8×10^{-3}	29	940	4.6	1.3×10^{-2}	31
920	4.8	6.5×10^{-3}	30	920	4.8	6.5×10^{-3}	30

Funding

National Institutes of Health (MH111359, NS057198, S10RR029050, U01NS094232); National Science Foundation (CBET 1445158, ECCS 1405234, ECCS 1507146); Office of Naval Research (ECE4509); Cymer.

Acknowledgments

We thank Drs. Sergei A. Vinogradov and Luca Ravotto for their help in interpreting the experimental results and discussions of the theory of two-photon absorption in molecules. We also thank Dr. Kaspar Podgorski for kindly providing us with the tissue heating simulation code and helping us with the code implementation. We thank Drs. Andrew Dunn and David Miller for sharing numeric data from their publication.

References

1. W. Denk, J. H. Strickler, and W. W. Webb, "Two-photon laser scanning fluorescence microscopy," *Science* **248**(4951), 73–76 (1990).
2. W.-C. A. Lee, J. L. Chen, H. Huang, J. H. Leslie, Y. Amitai, P. T. So, and E. Nedivi, "A dynamic zone defines interneuron remodeling in the adult neocortex," *Proc. Natl. Acad. Sci.* **105**(50), 19968–19973 (2008).
3. Y. Okubo, S. Kakizawa, K. Hirose, and M. Iino, "Visualization of ip_3 dynamics reveals a novel AMPA receptor-triggered ip_3 production pathway mediated by voltage-dependent ca^{2+} influx in purkinje cells," *Neuron* **32**(1), 113–122 (2001).
4. A. A. Oliva, M. Jiang, T. Lam, K. L. Smith, and J. W. Swann, "Novel hippocampal interneuronal subtypes identified using transgenic mice that express green fluorescent protein in GABAergic interneurons," *J. Neurosci.* **20**(9), 3354–3368 (2000).
5. M. Mank, A. F. Santos, S. Drenberger, T. D. Mrcic-Flogel, S. B. Hofer, V. Stein, T. Hendel, D. F. Reiff, C. Levelt, and A. Borst et al., "A genetically encoded calcium indicator for chronic in vivo two-photon imaging," *Nat. Methods* **5**(9), 805–811 (2008).
6. N. L. Rochefort and A. Konnerth, "Genetically encoded ca^{2+} sensors come of age," *Nat. Methods* **5**(9), 761–762 (2008).
7. S. Sakadžić, E. Roussakis, M. A. Yaseen, E. T. Mandeville, V. J. Srinivasan, K. Arai, S. Ruvinskaya, A. Devor, E. H. Lo, S. A. Vinogradov, and D. A. Boas, "Two-photon high-resolution measurement of partial pressure of oxygen in cerebral vasculature and tissue," *Nat. Methods* **7**(9), 755–759 (2010).
8. A. Devor, S. Sakadžić, P. A. Saisan, M. A. Yaseen, E. Roussakis, V. J. Srinivasan, S. A. Vinogradov, B. R. Rosen, R. B. Buxton, A. M. Dale, and D. A. Boas, "Overshoot of o_2 is required to maintain baseline tissue oxygenation at locations distal to blood vessels," *J. Neurosci.* **31**(38), 13676–13681 (2011).
9. D. Kleinfeld, P. P. Mitra, F. Helmchen, and W. Denk, "Fluctuations and stimulus-induced changes in blood flow observed in individual capillaries in layers 2 through 4 of rat neocortex," *Proc. Natl. Acad. Sci.* **95**(26), 15741–15746 (1998).
10. S. Nagayama, S. Zeng, W. Xiong, M. L. Fletcher, A. V. Masurkar, D. J. Davis, V. A. Pieribone, and W. R. Chen, "In vivo simultaneous tracing and ca^{2+} imaging of local neuronal circuits," *Neuron* **53**(6), 789–803 (2007).
11. E. M. Callaway, "A molecular and genetic arsenal for systems neuroscience," *Trends Neurosci.* **28**(4), 196–201 (2005).
12. P. Mahou, M. Zimmerley, K. Loulier, K. S. Matho, G. Labroille, X. Morin, W. Supatto, J. Livet, D. Débarre, and E. Beaupaire, "Multicolor two-photon tissue imaging by wavelength mixing," *Nat. Methods* **9**(8), 815–818 (2012).
13. S. Quentmeier, S. Denicke, and K.-H. Gericke, "Two-color two-photon fluorescence laser scanning microscopy," *J. Fluoresc.* **19**(6), 1037–1043 (2009).
14. E. P. Perillo, J. W. Jarrett, Y.-L. Liu, A. Hassan, D. C. Fernée, J. R. Goldak, A. Bonteanu, D. J. Spence, H.-C. Yeh, and A. K. Dunn, "Two-color multiphoton in vivo imaging with a femtosecond diamond raman laser," *Light: Sci. Appl.* **6**(11), e17095 (2017).
15. M. O. Cambaliza and C. Saloma, "Advantages of two-color excitation fluorescence microscopy with two confocal excitation beams," *Opt. Commun.* **184**(1-4), 25–35 (2000).
16. C. M. Blanca and C. Saloma, "Two-color excitation fluorescence microscopy through highly scattering media," *Appl. Opt.* **40**(16), 2722–2729 (2001).
17. C. Wang, L. Qiao, Z. Mao, Y. Cheng, and Z. Xu, "Reduced deep-tissue image degradation in three-dimensional multiphoton microscopy with concentric two-color two-photon fluorescence excitation," *J. Opt. Soc. Am. B* **25**(6), 976–982 (2008).
18. D. Kobat, G. Zhu, and C. Xu, "Background reduction with two-color two-beam multiphoton excitation," in *Biomedical Optics*, (Optical Society of America, 2008), p. BMF6.
19. S. Lindek and E. Stelzer, "Resolution improvement by nonconfocal theta microscopy," *Opt. Lett.* **24**(21), 1505–1507 (1999).
20. C. Ibáñez-López, I. Escobar, G. Saavedra, and M. Martínez-Corral, "Optical-sectioning improvement in two-color excitation scanning microscopy," *Microsc. Res. Tech.* **64**(2), 96–102 (2004).
21. D. R. Miller, J. W. Jarrett, A. M. Hassan, and A. K. Dunn, "Deep tissue imaging with multiphoton fluorescence microscopy," *Curr. Opin. Biomed. Eng.* **4**, 32–39 (2017).
22. M.-H. Yang, M. Abashin, P. A. Saisan, P. Tian, C. G. Ferri, A. Devor, and Y. Fainman, "Non-degenerate 2-photon excitation in scattering medium for fluorescence microscopy," *Opt. Express* **24**(26), 30173–30187 (2016).
23. C. Xu and W. W. Webb, "Measurement of two-photon excitation cross sections of molecular fluorophores with data from 690 to 1050 nm," *J. Opt. Soc. Am. B* **13**(3), 481–491 (1996).
24. B. P. Cormack, R. H. Valdivia, and S. Falkow, "FACS-optimized mutants of the green fluorescent protein (gfp)," *Gene* **173**(1), 33–38 (1996).
25. A. Sakaue-Sawano, H. Kurokawa, T. Morimura, A. Hanyu, H. Hama, H. Osawa, S. Kashiwagi, K. Fukami, T. Miyata, H. Miyoshi, T. Imamura, M. Ogawa, H. Masai, and A. Miyawaki, "Visualizing spatiotemporal dynamics of multicellular cell-cycle progression," *Cell* **132**(3), 487–498 (2008).
26. R. Sjöback, J. Nygren, and M. Kubista, "Absorption and fluorescence properties of fluorescein," *Spectrochim. Acta, Part A* **51**(6), L7–L21 (1995).

27. G. Reynolds and K. H. Drexhage, "New coumarin dyes with rigidized structure for flashlamp-pumped dye lasers," *Opt. Commun.* **13**(3), 222–225 (1975).
28. A. Nimmerjahn, F. Kirchhoff, J. N. Kerr, and F. Helmchen, "Sulforhodamine 101 as a specific marker of astroglia in the neocortex in vivo," *Nat. Methods* **1**(1), 31–37 (2004).
29. S. Sadegh, M.-H. Yang, C. G. Ferri, M. Thunemann, P. A. Saisan, A. Devor, and Y. Fainman, "Measurement of the relative non-degenerate two-photon absorption cross-section for fluorescence microscopy," *Opt. Express* **27**(6), 8335–8347 (2019).
30. M. Drobizhev, N. S. Makarov, S. E. Tillo, T. E. Hughes, and A. Rebane, "Two-photon absorption properties of fluorescent proteins," *Nat. Methods* **8**(5), 393–399 (2011).
31. J. Mütze, V. Iyer, J. J. Macklin, J. Colonell, B. Karsh, Z. Petrášek, P. Schwille, L. L. Looger, L. D. Lavis, and T. D. Harris, "Excitation spectra and brightness optimization of two-photon excited probes," *Biophys. J.* **102**(4), 934–944 (2012).
32. S. de Reguardati, J. Pahapill, A. Mikhailov, Y. Stepanenko, and A. Rebane, "High-accuracy reference standards for two-photon absorption in the 680–1050 nm wavelength range," *Opt. Express* **24**(8), 9053–9066 (2016).
33. R. R. Birge and B. M. Pierce, "Semiclassical time-dependent theory of two-photon spectroscopy. the effect of dephasing in the virtual level on the two-photon excitation spectrum of isotachysterol," *Int. J. Quantum Chem.* **29**(4), 639–656 (1986).
34. J. M. Hales, D. J. Hagan, E. W. Van Stryland, K. Schafer, A. Morales, K. D. Belfield, P. Pacher, O. Kwon, E. Zojer, and J.-L. Brédas, "Resonant enhancement of two-photon absorption in substituted fluorene molecules," *J. Chem. Phys.* **121**(7), 3152–3160 (2004).
35. M. Drobizhev, N. S. Makarov, A. Rebane, G. de la Torre, and T. Torres, "Strong two-photon absorption in push-pull phthalocyanines: Role of resonance enhancement and permanent dipole moment change upon excitation," *J. Phys. Chem. C* **112**(3), 848–859 (2008).
36. H. S. Pattanaik, M. Reichert, J. B. Khurgin, D. J. Hagan, and E. W. Van Stryland, "Enhancement of two-photon absorption in quantum wells for extremely nondegenerate photon pairs," *IEEE J. Quantum Electron.* **52**(3), 1–14 (2016).
37. K. Podgorski and G. Ranganathan, "Brain heating induced by near-infrared lasers during multiphoton microscopy," *J. Neurophysiol.* **116**(3), 1012–1023 (2016).
38. N. C. Shaner, P. A. Steinbach, and R. Y. Tsien, "A guide to choosing fluorescent proteins," *Nat. Methods* **2**(12), 905–909 (2005).
39. K. M. Dean and A. E. Palmer, "Advances in fluorescence labeling strategies for dynamic cellular imaging," *Nat. Chem. Biol.* **10**(7), 512–523 (2014).
40. G. McNamara, M. Dfilippantonio, T. Ried, and F. R. Bieber, "Microscopy and image analysis," *Curr. Protoc. Hum. Genet.* **46**(1), 441–4434 (2005).
41. W. L. Peticolas, "Multiphoton spectroscopy," *Annu. Rev. Phys. Chem.* **18**(1), 233–260 (1967).
42. J. Bhawalkar, G. He, and P. Prasad, "Nonlinear multiphoton processes in organic and polymeric materials," *Rep. Prog. Phys.* **59**(9), 1041–1070 (1996).
43. T. V. Esipova, H. J. Rivera-Jacquez, B. Weber, A. E. Masunov, and S. A. Vinogradov, "Two-photon absorbing phosphorescent metalloporphyrins: effects of π -extension and peripheral substitution," *J. Am. Chem. Soc.* **138**(48), 15648–15662 (2016).
44. C. W. Dirk, L.-T. Cheng, and M. G. Kuzyk, "A simplified three-level model describing the molecular third-order nonlinear optical susceptibility," *Int. J. Quantum Chem.* **43**(1), 27–36 (1992).
45. A. Rebane, M. Drobizhev, N. Makarov, E. Beuerman, S. Tillo, and T. Hughes, "New all-optical method for measuring molecular permanent dipole moment difference using two-photon absorption spectroscopy," *J. Lumin.* **130**(9), 1619–1623 (2010).
46. A. Rebane, G. Wicks, M. Drobizhev, T. Cooper, A. Trummal, and M. Uudsemaa, "Two-photon voltmeter for measuring a molecular electric field," *Angew. Chem., Int. Ed.* **54**(26), 7582–7586 (2015).
47. N. G. Horton, K. Wang, D. Kobat, C. G. Clark, F. W. Wise, C. B. Schaffer, and C. Xu, "In vivo three-photon microscopy of subcortical structures within an intact mouse brain," *Nat. Photonics* **7**(3), 205–209 (2013).